POLITECNICO DI TORINO
Repository ISTITUZIONALE

Development, characterization and optimization of a new bone cement based on calcium–strontium aluminates and chitosan-glycerin solution

Original
Development, characterization and optimization of a new bone cement based on calcium–strontium aluminates and chitosan-glycerin solution / Souza, M.K.S., Lima, E.P.N., Nascimento, I.V.S.R., Montazerian, M., Baino, F., Fook, M.V.L.. - In: CERAMICS INTERNATIONAL. - ISSN 0272-8842. - ELETTRONICO. - 48:21(2022), pp. 31866-31879. [10.1016/j.ceramint.2022.07.120]

Availability:
This version is available at: 11583/2977787 since: 2023-04-05T15:57:37Z

Publisher:
Elsevier Ltd

Published
DOI:10.1016/j.ceramint.2022.07.120

Terms of use:

This article is made available under terms and conditions as specified in the corresponding bibliographic description in the repository

Publisher copyright
Elsevier postprint/Author's Accepted Manuscript

© 2022. This manuscript version is made available under the CC-BY-NC-ND 4.0 license http://creativecommons.org/licenses/by-nc-nd/4.0/.The final authenticated version is available online at: http://dx.doi.org/10.1016/j.ceramint.2022.07.120

(Article begins on next page)

17 November 2026

Development, Characterization and Optimization of a New Bone Cement Based on Calcium-Strontium Aluminates and Chitosan-Glycerin Solution

Mairly K. S. Souza[1,*], Eunice P. N. Lima[1], Imarally V. S. R. Nascimento[2], Maziar Montazerian[1,*], Francesco Baino[3], Marcus V. L. Fook[1,*]

1- Northeastern Laboratory for Evaluation and Development of Biomaterials (CERTBIO), Federal University of Campina Grande, PB, Brazil.
2- Center for Science and Technology in Energy and Sustainability (CETENS), Federal University of Recôncavo of Bahia, BA, Brazil.
3- Institute of Materials Physics and Engineering, Applied Science and Technology Department, Politecnico di Torino, Torino, Italy.

*Corresponding authors: M.K.S. Souza (mairlykarolyne@gmail.com), M. Montazerian (maziar_montaz@yahoo.com) and M.V.L. Fook (marcus.liafook@certbio.ufcg.edu.br)

Abstract

Bioceramic bone cements are increasingly studied, developed, and improved to become a viable alternative to polymethyl methacrylate (PMMA)-based cements. In this regard, we aimed to develop a new cement composed of calcium aluminate ($C_{12}A_7$) and strontium aluminate (S_3A) powders obtained via solution combustion synthesis (SCS) and chitosan/glycerin solution. The cement properties were optimized through a design of experiments. The approach used in the optimization process was the 2^k factorial experimental design with insertion of 3 repetitions of the central point, which resulted in 11 compositions. All compositions were tested to determine the liquid/powder ratio (L/P), final setting time (ST), maximum hydration temperature (T_{max}), compressive strength and radiopacity. The results were statistically evaluated by analyzing the effects, Pareto diagram, ANOVA analysis and response surface plot. The models obtained in this study could precisely predict three responses: T_{max}, compressive strength, and radiopacity. An optimized composition for possible application as bone cement had an average T_{max} of 40.34 ºC, compressive strength of 7.75 MPa and radiopacity of 3.76 mm Al, all above the standard requirements.

Keywords: Bone cement; Calcium aluminate; Strontium aluminate; Chitosan; Optimization.

1. Introduction

Cements are obtained by mixing a powder phase with a liquid phase, forming a moldable paste that hardens over time [1]. In orthopedics, bone cements are commonly used in hip arthroplasty surgeries. Their main functions include transferring body weight and service loads from the prosthesis to the bone and the immediate fixation of the prosthesis to host bone [2]. Polymethyl methacrylate (PMMA) is widely used in this application despite its several disadvantages, such as the high polymerization temperature (66 to 120 ºC) and incomplete polymerization of methyl methacrylate (MMA) monomer leading to thermal and chemical necrosis, compromised blood circulation, and induction of hypotensive effects which are collectively called as "cement disease". In addition, PMMA cement per se promotes neither bone growth nor osteointegration which may contribute to the failure of the surgical procedure [2,1,3].

As an alternative to the use of PMMA cements, bioceramic cements such as calcium phosphates (CPCs) and calcium sulfates emerged over the last decades and have been cleared for clinical applications [4]. They mimic, to some extent, the inorganic phase of bones and teeth and are biocompatible, bioactive, osteoconductive and osteoinductive [5,6,7]. Their main drawback is the lower mechanical strength compared to polymeric cements [8]. Calcium aluminate cements (CACs) could overcome this limitation by forming calcium-rich and aluminum-rich hydrates, conducive to improving bioactivity and mechanical properties, respectively [9]. Among the crystalline phases available in the CaO-Al_2O_3 binary system, the dodecacalcium hepta-aluminate ($12CaO \cdot 7Al_2O_3$, $C_{12}A_7$) stands out for being rapidly hydrated due to its high CaO content. Therefore, it is considered for controlling the aging time of commercial cement [10].

Bioceramics can be produced through several methods, some of which are the synthesis by a solid-state reaction [11], chemical precipitation [12], sol-gel [13], hydrothermal processes [14], and solution combustion synthesis (SCS) [15]. The SCS provides time/energy savings in preparing a variety of advanced ceramics, catalysts and nanomaterials with high reactivity and controlled morphology. It involves a fast and self-sustaining redox reaction between a fuel and an oxidant in the presence of metallic cations [16,17,18,19]. This technique is valuable because of its simplicity and cost-effectiveness.

Chitosan, which is employed as a component of bone cements both in the liquid phase [20] and the powder form [21], is a biopolymer derived from the deacetylation of chitin and is known for its biocompatibility as well as antibacterial and antifungal activities. The liquid

chitosan can be distributed evenly throughout the cement, providing adequate cohesion and better surgical handling properties without altering the mechanical properties or delaying the early hardening of the cements [20]. Plasticizing agents like glycerin can modulate the cement properties by improving consistency between organic and inorganic phases, adjusting the injectability and increasing the setting time [22, 23]. Also, it can be stored at room temperature without drying out and has been frequently used in clinical applications [24, 25]. Therefore, glycerin is widely used in conjunction with chitosan in many applications [26].

An important physical property of bone cements is radiopacity, as it allows clinical evaluation of materials at the surgical site. The literature has reported the use of several radiopacifying agents in cements, such as bismuth oxide (Bi_2O_3) [27], zirconium dioxide (ZrO_2) [28], barium sulphate ($BaSO_4$) [29], ytterbium fluoride (YbF_3) [30], calcium tungstate ($CaWO_4$) [31], niobium pentoxide (Nb_2O_5) [28], etc [32]. Strontium (Sr)-containing materials are also radiopaque. For example, tri-strontium aluminate ($3SrO{\cdot}Al_2O_3$, S_3A), the most Sr-abundant phase in the SrO-Al_2O_3 binary system, is radiopaque. When hydrated, it also forms a cement paste with a short handling and hardening time [33,34,35]. Although this phase differs from its calcium counterpart by being more radiopaque, its potential use as a radiopacifying agent in biomedical cements has been poorly reported.

An appropriate cement should meet several essential requirements before being considered for biomedical application. Briefly, it should be easy to handle, shapeable/mouldable, have reasonable setting time, a hydration temperature close to body temperature, not disintegrate when in contact with physiological fluids, have adequate mechanical resistance, be biocompatible and radiopaque [1]. Unfortunately, there is no ideal bone cement available on the market that meets all the requirements above and, therefore, there is room for further improvement.

Bone cement optimization can follow a cook-and-look or a more rational approach. In this regard, the design of experiments (DOE) is widely used to design production processes. The DOE contributes to achieving the expected property with statistical validity combined with an efficient number of experiments. By employing this technique, it is possible to obtain a mathematical model that relates the behavior of the responses to the process input variables, allowing their reliable optimization [36].

The present work aimed to develop a new cement composed of $C_{12}A_7$ and S_3A obtained via SCS (powder phase) and chitosan/glycerin solution (liquid phase). DOE was also applied to optimize the responses like handling properties, final setting time (ST), maximum hydration temperature (T_{max}), compressive strength, and radiopacity.

2. Materials and Methods

2.1. Synthesis of $C_{12}A_7$ and S_3A powders

$C_{12}A_7$ and S_3A powders were prepared via SCS. The reagents used in the synthesis of $C_{12}A_7$ were calcium nitrate tetrahydrate ($Ca(NO_3)_2.4H_2O$, purity (P) ≥ 99%, Neon), aluminum nitrate nonahydrate ($Al(NO_3)_2.9H_2O$, P ≥ 98%, Neon) and urea ($(NH_2)_2CO$, P ≥ 97%, Neon). Strontium carbonate ($SrCO_3$, P ≥ 98%, Sigma-Aldrich), aluminum nitrate nonahydrate ($Al(NO_3)_2.9H_2O$, P ≥ 98%, Neon), nitric acid (HNO_3 65%, Sigma-Aldrich) and urea ($(NH_2)_2CO$, P ≥ 97%, Neon) were used for the synthesis of S_3A.

$C_{12}A_7$ and S_3A powders were obtained following the methodologies described by Rodríguez *et al.* [37] and Barbosa *et al.* [33], respectively, using the stoichiometry amount of reagents necessary for each synthesis. The following equations summarize the sequence of reactions in the synthesis process of $C_{12}A_7$ (Eq. (1)) and S_3A (Eqs. (2) and (3)).

$$12Ca(NO_3)_2.4H_2O_{(aq)} + 14Al(NO_3)_3.9H_2O_{(aq)} + 55(NH_2)_2CO_{(aq)} \rightarrow Ca_{12}Al_{14}O_{33(s)}\ (i.e.\ 12\mathrm{CaO}\cdot 7Al_2O_3, C_{12}A_7) + 88N_{2(g)} + 55CO_{2(g)} + 284H_2O_{(g)} \quad (1)$$

$$SrCO_{3(s)} + 2HNO_{3(aq)} \rightarrow Sr(NO_3)_{2(aq)} + H_2O_{(g)} + CO_{2(g)} \quad (2)$$

$$3Sr(NO_3)_{2(s)} + 2Al(NO_3)_3.9H_2O_{(aq)} + 10(NH_2)_2CO_{(aq)} \rightarrow Sr_3Al_2O_{6(s)}\ (i.e.\ 3SrO\cdot Al_2O_3, S_3A) + 38H_2O_{(g)} + 10CO_{2(g)} + 16N_{2(g)} \quad (3)$$

Briefly, in order to obtain 5 g of each aluminate, the stoichiometric amounts of the reagents were dissolved in 50 mL of ultrapure water (for the synthesis of $C_{12}A_7$) and 50 mL of HNO_3 (for the synthesis of S_3A), under magnetic stirring at a constant temperature of 82 ± 1 ºC, until a reduction of ¾ of the initial volume was observed. After that, the solutions were put in an oven at 600 ºC for 10 min, which was enough time for the complete combustion process to occur. Finally, the combustion products were removed from the oven, cooled to room temperature, hand-crushed in a mortar and passed through a 400-mesh stainless steel sieve.

2.2. Characterization of $C_{12}A_7$ and S_3A powders

2.2.1. Crystalline phases

The crystalline phases of the ceramic powders were evaluated using the X-ray diffraction (XRD) technique. An XRD 7000 diffractometer (Shimadzu) was used, with a voltage of 40 kV, current of 30 mA and copper K_α radiation (λ = 1.5418 Å). The scan angles were from 5 to 60º (2θ), with a step size of 0.02º and a time per step of 1.2 seconds. The Rietveld refinement method was used to quantify the amount of each phase.

2.2.2. Microstructural analysis

The shape and surface morphology of the powders were analyzed by a scanning electron microscope (SEM, Hitachi TM-1000), working with voltage and current of 15 kV and 30 mA, respectively. To observe the morphology of the powders obtained after SCS, the microstructural analysis was carried out on pristine powders that were not crushed in a mortar or passed through a 400 mesh sieve but only de-agglomerated.

2.2.3. Average particle size distribution

The average particle size distribution (d_{50}) was determined using a Mastersizer 2000 analyzer (Malvern Instruments). This analyzer detects particles dispersed in a liquid with a size range of 0.02 to 2000 μm through laser diffraction technology. Specifically, 5 g of each powder were dispersed in 250 mL of distilled water by a mechanical stirrer for 1 minute.

2.3. Preparation of cements

The cement preparation was based on a 2^k factorial experimental design, with 3 repetitions of the central point. K corresponds to the number of input variables considered in the planning. X1 denotes the amount of S_3A in the solid phase of the cement, X2 is the amount of the chitosan in the liquid phase, and X3 quantifies the ratio of the glycerin to chitosan (see Table 1). The amount of $C_{12}A_7$ was not considered an input variable because it is inversely related to the amount of S_3A.

Table 1. 2^k factorial experimental design, displaying the input variables and their respective codes, measurement units, limits (lower and upper) and center points.

Variables	Codes	Units	(-)	0	(+)
S_3A	X1	wt.% in the solid phase of the cement	20	50	80
Chitosan	X2	wt.% in the solution	0.5	1.0	1.5
Glycerin	X3	Glycerin to chitosan ratio in the solution	5:1	10:1	15:1

The cements were prepared by mixing the solid and liquid phases until a homogeneous and consistent paste was obtained. The solid phases consisted of different proportions of $C_{12}A_7$ and S_3A (X1) and the liquid phases consisted of solutions of chitosan (X2) with glycerin (X3) of different concentrations. Glycerin was increased in the solutions to act as a coupling agent between the organic and inorganic phases of the cements [21, 22]. Altogether 11 cement compositions were prepared, whose preparation conditions are listed in Table 2, that is, the coded values (-), (0) and (+) of the amounts of X1, X2 and X3; and, in Table 1, the values corresponding to these codes are reported. Chitosan with glycerin solutions for cement hydration were prepared using medium molecular weight chitosan (230–250 KDa) (medical grade, CERTBIO) and glycerin ($C_3H_8O_3$, ≥ 99%, Neon), completely solubilizing in acetic acid solution (1% v/v) (CH_3CO_2H, ≥ 99.8%, Neon), under magnetic stirring for 2 hours.

Table 2. Instructions on the quantities of each component necessary for the formation of cements.

	Codes of variables (see Table 1)		
Cements	X1	X2	X3
1	-	-	-
2	+	-	-
3	-	+	-
4	+	+	-
5	-	-	+
6	+	-	+
7	-	+	+
8	+	+	+
9	0	0	0
10	0	0	0
11	0	0	0

2.4. Characterization of cements

The cements were evaluated for their liquid/powder ratio (L/P), setting time (ST), maximum hydration temperature (T_{max}), comprehensive strength and radiopacity.

2.4.1. Liquid/powder ratio (L/P)

The liquid/powder (L/P) ratio for each cement composition was empirically determined. One gram (1 g) of the cement powder was placed in a Petri dish. Then, with the aid of a digital micropipette, the chitosan and glycerin solution were added to the powder while mixing it until obtaining a homogeneous paste suitable for clinical handling. In this way, it was possible to fix the amount of solution necessary to get a cement with the desired consistency and determine the L/P ratio for each composition.

2.4.2. Setting time (ST)

The setting time (ST) is defined by the time elapsed between the initial mixing of the powder and liquid phases until hardening. The determination of ST was based on the guidelines of ISO/DIS 18531-2015 [38]. The cements were prepared by mixing the paste for 60 s. Then, the samples were placed in a mold made of acrylonitrile-butadiene-styrene (ABS) of 10 mm in diameter and 5 mm in height. The molds, together with the Vicat apparatus, were placed in an oven with controlled temperature (37 ± 2 ºC) and humidity (95-100%). The Vicat apparatus consisted of a moving part that weighed 300 ± 1 g and a steel needle with dimensions of 43 ± 1 mm in height and 1.13 ± 0.05 mm in diameter. After 2 min of mixing the cements, the mold was placed below the Vicat needle. This process continued every 2 min until the needle no longer made an impression on the cement surface. This test was repeated three times for each composition.

2.4.3. Maximum setting temperature (T_{max})

An exothermic chemical reaction occurs when the powder and liquid phases are mixed to form a cement. The cement heats up to a maximum peak temperature (T_{max}) and then cools down to the initial temperature (24 ºC). The T_{max} measurements were performed with a high precision thermometer/data logger, model HH806AU Omega^{TM}, USA, with a type K

thermocouple (measuring range from -200 to 1372 ºC). The cements were prepared by mixing for 60 seconds, then the thermocouple was inserted into the paste, and the set was eventually placed inside a styrofoam box to prevent heat exchange with the external environment during the hydration reaction. The temperature was recorded every 2 seconds and the test was repeated three times for each composition.

2.4.4. Compressive strength

This test was performed based on the guidelines provided by the ABNT NBR ISO 5833:2004 [39]. The cements were prepared by mixing the precursors for 60 seconds. Then, the specimens were made by pouring the cement paste into molds of 6 mm in diameter and 12 mm in height. After 48 hours, the specimens were demolded and submitted to the compression test. The tests were carried out on a universal testing machine, model 3360 Series Dual Column Table Frames, Instron, USA, with a load cell of 500 N and a constant crosshead speed of 0.5 mm/min. The tests were carried out on five specimens for each of the 11 compositions.

2.4.5. Radiopacity evaluation

The procedures adopted to carry out this analysis were based on the ABNT NBR ISO 13116:2020 standard [40]. For clinical purposes, the radiopacity of cement must be equal to or greater than 3 millimeters of aluminum (mm Al).

The cements were prepared and placed in disk-shaped molds with dimensions of 10 ± 1 mm in diameter and 1.5 ± 0.5 mm in thickness, being demolded after 24 hours. The test was performed simultaneously on 3 samples for each composition, thus determining their average radiopacity. The equipment used to obtain the digital radiographic images was an X-ray tube, model IMAGE (Dabi Atlante), operating at 70 kV, 8 mA, with a standard exposure time of 0.25 seconds. The samples were placed on a phosphor plate with an aluminum scale of purity greater than 95%, with increments of 1 mm in thickness. The entire set (samples, aluminum scale, and phosphor plate) were positioned 30 centimeters away from the X-ray tube.

The digital radiographic images were analyzed using the Image J® software (National Institute of Health, USA), where an optical density tool was applied in order to identify the density of the areas of the images. The average gray level of the respective aluminum steps was defined and a calibration curve of the "thickness (mm) of the step" vs. "average gray level" was

generated with an R^2 of 98.7%. In this way, it was possible to express the radiopacity of the cements in mm Al.

2.5. Statistical analysis and optimization approach

The results were expressed as average ± standard deviation and statistically analyzed using MINITAB® 19 and STATISTICA® 10 softwares (significance level of 5%). MINITAB® 19 was used to determine the influence of effects, ANOVA analysis and obtain the model equation. STATISTICA® 10 was used to construct Pareto diagrams and response surface plots. The response surface methodology allows establishing the role played by important factors and the interactions of such variables in the process. The goal is the optimization of the response based on the factors evaluated.

2.6. Characterization of optimized cement

After the statistical analysis performed on the results acquired through the cement characterizations, it was possible to find a cement with optimized composition. This cement was characterized in terms of phase evolution, chemical groups and morphology. These characterizations were performed after 24 h of hydration. In addition, the validation of the mathematical equations obtained from the statistical models was performed.

2.6.1. Phase formation in the cement

The phases in optimized composition were identified using the XRD technique.

2.6.2. Evaluation of chemical groups

The FTIR analysis was performed to identify the chemical groups present in the cement of optimized composition. The spectrum was acquired on a Spectrum 400 Spectrometer (Perkin Elmer, Massachusetts) coupled with attenuated total reflectance (ATR) accessories equipped with a thallium bromoiodide (KRS-5) crystal in a range of 4000–400 cm^{-1}, and through 32 scans with a resolution of 4 cm^{-1}. Before data collection, the sample was dried at 40 ºC for 1 h to remove moisture.

2.6.3. Microstructural evaluation

The microstructure of the optimized cement composition was evaluated by SEM, following the same methodology described in section 2.2.2.

3. Results and Discussion

3.1. Characterization of $C_{12}A_7$ and S_3A powders

3.1.1. XRD

Figure 1 shows the XRD patterns of the $C_{12}A_7$ and S_3A powders synthesized by SCS method. In $C_{12}A_7$, two crystalline phases were identified. The main phase was dodecacalcium hepta-aluminate ($12CaO{\cdot}7Al_2O_3$, $C_{12}A_7$), characterized (according to ICSD 01-070-2144) by two very intense peaks at 18.11º and 33.39º. The second phase was tricalcium aluminate ($3CaO{\cdot}Al_2O_6$, C_3A) of cubic structure, with characteristic peaks in conformity with ICSD (01-070-0839). These phases were quantified by the Rietveld refinement technique, with 84.71% corresponding to $C_{12}A_7$ and 15.29% to C_3A. The C_3A phase was also detected by Barbosa *et al*. [41] after employing the SCS technique to obtain $C_{12}A_7$. It has been reported that the stable region of $C_{12}A_7$ formation in the CaO-Al_2O_3 phase diagram is relatively narrow, making it possible for C_3A to form by any composition deviation [42]. The C_3A phase is more reactive than $C_{12}A_7$ due to the greater amount of CaO: in fact, the former has a higher CaO/Al_2O_3 ratio (3:1) than the latter (12:7). Despite being present in a lower percentage than the $C_{12}A_7$ phase, the C_3A phase, due to its high reactivity, may favor faster and more intense hydration of the cement [10], which would accelerate the curing process, thus reducing the time necessary for cement reaches higher levels of mechanical strength.

XRD pattern of S_3A (Figure 1) showed the existence of three phases. The main phase consists of the desired phase, tri-strontium aluminate ($3SrO{\cdot}Al_2O_3$, S_3A) of cubic structure, with the main characteristic peak near 31.92º and others of lower intensities at 56.89º and 45.77º (ICSD, 01-079-1094). The second phase was monoclinic strontium aluminate ($SrO{\cdot}Al_2O_3$, SA), with prominent characteristic peaks at 29.29º, 28.38º and 20.13º (ICSD 01-074-0794). The third phase was attributed to strontium carbonate ($SrCO_3$), with an orthorhombic structure (ICSD, 01-071-2393). The amount of each phase, i.e., 77.24% S_3A, 17.29% SA and 5.47% $SrCO_3$, was determined by the Rietveld refinement method.

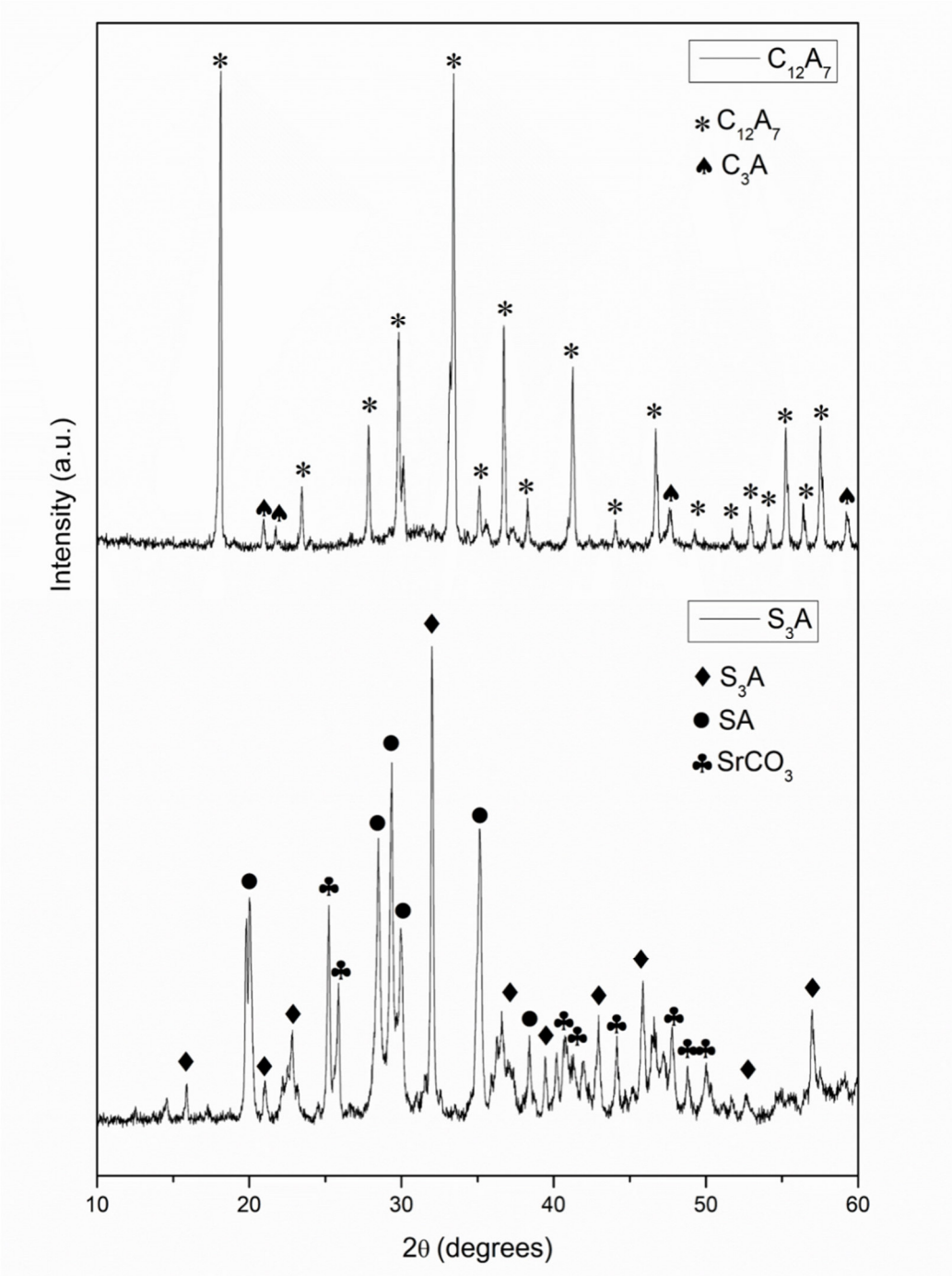


Figure 1. XRD patterns of $C_{12}A_7$ and S_3A powders synthesized using the SCS method.

In the $SrO\text{-}Al_2O_3$ phase diagram, the SA phase is close to the S_3A. Rojas-Hernandez *et al.* [43] have argued that the formation of crystalline phases with different Sr/Al ratios indicates a lack of homogeneity in the system during the combustion process. The authors further elucidated that the SA is formed at higher temperatures than the S_3A, which, in this case, happens when the combustion temperature exceeds 500 ºC. Therefore, using the above

stoichiometric amount of urea and combustion temperature of 600 ºC led to the formation of a amount of SA. A amount of unreacted $SrCO_3$ was also detected. According to Ptáček *et al.* [35], during the synthesis of strontium aluminate, SA covers the $SrCO_3$ surface and retards its thermal decomposition by inhibiting the diffusion of CO_2 from the core to the reaction interface of $SrCO_3$.

3.1.2. Morphological investigation

Figure 2 shows the SEM images of $C_{12}A_7$ and S_3A powders obtained via SCS. The solid products show particles of different sizes and morphologies. Similar results have also been reported by Cao *et al.* [44], which described that an SCS process yields agglomerated particles, fine flakes and granules with a porous, spongy appearance; the last case is originated by the considerable volume of gases released during the reaction. Additionally, Novitskaya *et al.* [45] demonstrated that the higher the amount of gases produced during combustion reactions, the lower the tendency towards agglomeration, thus increasing the specific surface area. Some agglomerates present more uniform, homogeneous surfaces among the different morphologies observed. According to Rodríguez *et al.* [37], they are made up of nanometric grains, which end up being sintered due to the high combustion temperature.

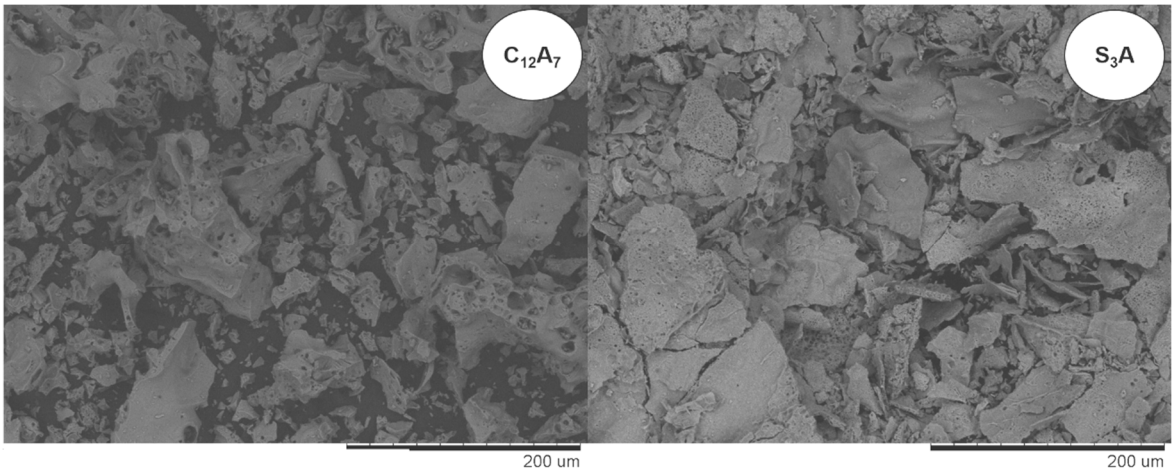


Figure 2. SEM images of the $C_{12}A_7$ and S_3A powders obtained at ×500 magnification.

3.1.3. Average particle size distribution

The average particle sizes (d_{50}) of $C_{12}A_7$ (Figure 3) and S_3A (Figure 4) powders were 24.4 and 13.7 μm, respectively. These sizes were larger than those observed by Barbosa *et al.*

[33] (8.2 and 3.1 µm for $C_{12}A_7$ and S_3A, respectively). This difference could be due to the processing method adopted. They chose to grind the powders for 10 min in a ball mill, whereas, in this study, the powders were hand-ground in a mortar and then sieved through a 400 mesh.

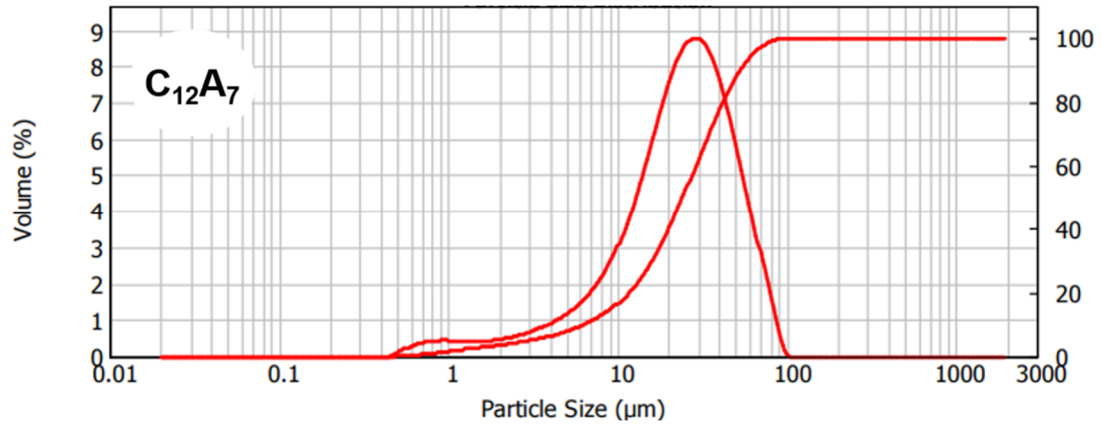


Figure 3. $C_{12}A_7$ particle size distribution.

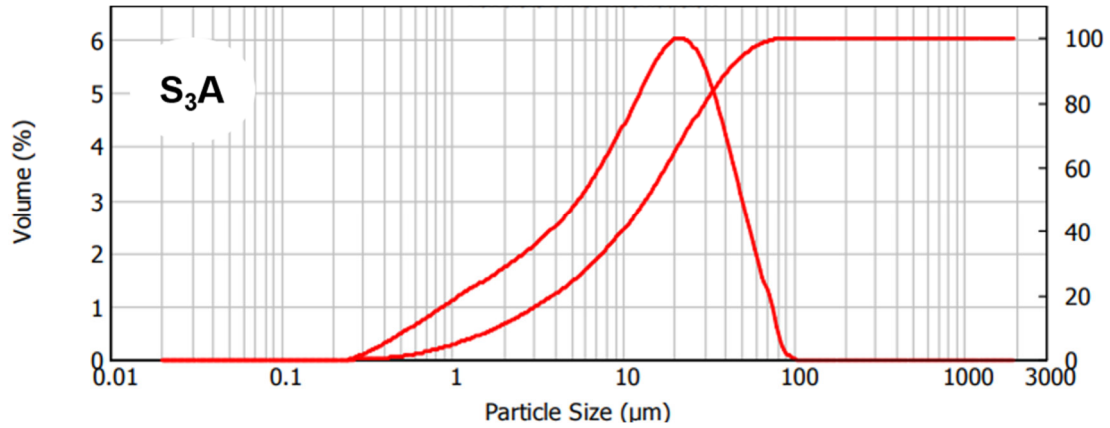


Figure 4. S_3A particle size distribution.

3.2. Characterization of cements

3.2.1. Determination of L/P, ST and T_{max}

To better understand the L/P, ST and T_{max} results, it is necessary to understand the setting mechanism during cement preparation. Briefly, the hydration process of aluminous cements initiates from the surface of the particles in contact with water [34]. The fixation mechanism of these cements is by dissolution and precipitation of ions. In the case of calcium aluminate cements (CAC), the dissolution of the anhydrous phases increases the concentration of Ca^{2+} and $Al(OH)_4^-$ ions in the solution, with a small part of $Al(OH)_4^-$ dissociating into Al^{3+}

and $4OH^-$. After a while, the concentration of these ions reaches the solubility limit in the solution, thus, the process of precipitation of a hydrated phase begins, favoring the dissolution of the anhydrous phases. This ion dissolution-precipitation process continues until most or all of the particles in the anhydrous phases of the cement in contact with water are consumed. However, the precipitation of a hydrated phase is preceded by a slow nucleation step, called the "induction period". This period lasts until the first hydrate nuclei are formed. After this stage, precipitation occurs quickly [46]. As with CAC, strontium aluminate cements (SrAC) also exhibit hydraulic behavior when in contact with water [34].

The L/P, ST and T_{max} values of the cements are listed in Table 3.

Table 3. L/P, ST and T_{max} of cemants.

Cements	L/P (ml/g)	ST (min)	T_{max} (ºC)
1	1.0	38	37.1
2	1.0	65	36.6
3	1.6	89	38.8
4	1.2	98	37.5
5	1.2	43	45.6
6	1.0	42	39.4
7	1.6	14	44.2
8	1.2	25	37.7
9	1.4	72	39.6
10	1.4	70	40.3
11	1.4	73	40.3

In order to produce cements with acceptable (empirically determined) workability, adding 1 to 1.6 ml of the liquid phase to 1 g of powder was necessary. The analysis of effects showed that only the variable "chitosan", with a p-value of 2.1%, exerted a statistically significant influence on the L/P response. The Pareto chart of standardized effects (Figure 5), which allows the visualization of the most significant process variables in each response, corroborated this result. A Pareto chart shows the magnitude and the importance of the effects. Bars that cross the reference line (here above p=0.05) are statistically significant on the Pareto chart. The influence of chitosan content can be observed in cements 3 and 7, where a greater amount of chitosan implied the need for more solution to achieve acceptable workability. Also, Leroux *et al.* [47] have shown that a high content (above 0.5 wt.%) of chitosan present in the

liquid phase of cements favors the agglomeration of particles and better cohesion between the grains.

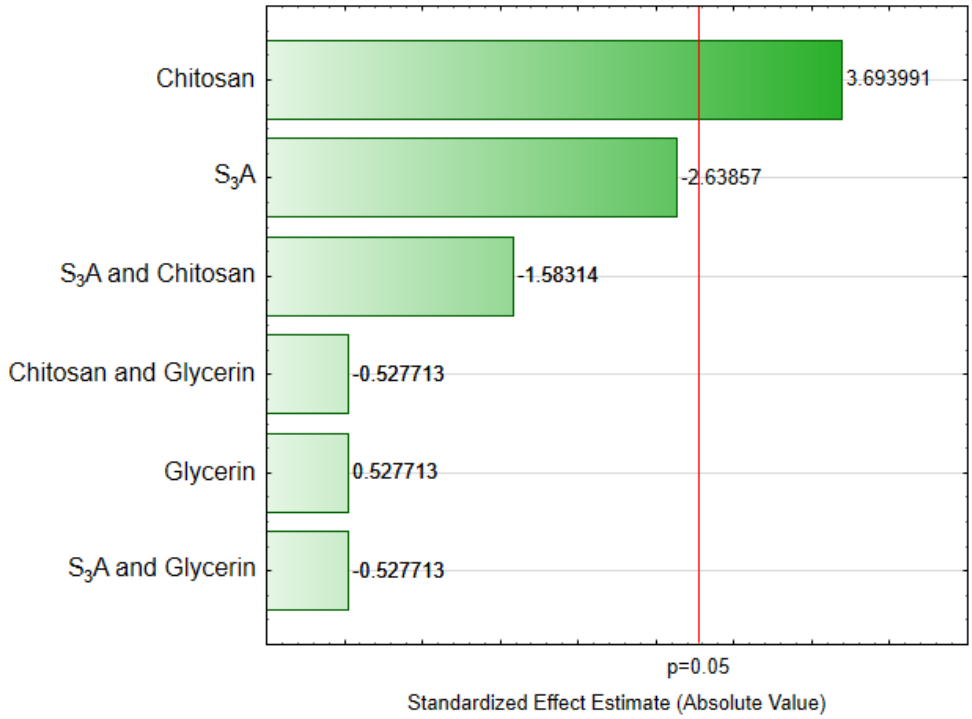


Figure 5. Pareto chart for the L/P ratio response. 2^3 design refers to the type of experimental planning adopted. 2 corresponds to the levels (+ and -) and, 3 to the process input variables (X1, X2 and X3) (Table 1). Mean square residual = 0.0179545.

The setting time of the cements ranged from 14 to 98 min. The analysis of effects showed that the "glycerin" and the interaction of the variables "chitosan and glycerin", with p-values of 2.0% and 4.3%, respectively, were statistically significant. The Pareto chart of standardized effects (Figure 6) confirmed this result.

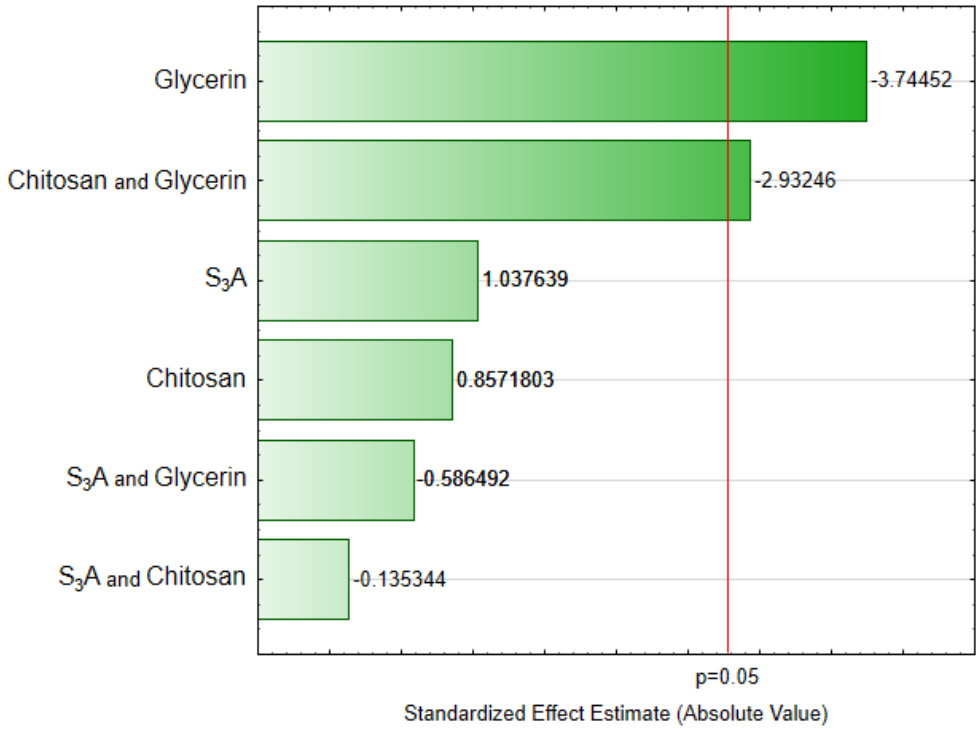


Figure 6. Pareto chart for the setting time (ST) response. 2^3 design refers to the type of experimental planning adopted. 2 corresponds to the levels (+ and -) and 3 to the process input variables (X1, X2 and X3) (Table 1). Mean square residual = 245.6591.

The lower the percentage of glycerin, the longer the setting time, as shown for cements 3 (89 min) and 4 (98 min). The opposite occurred with those with a higher percentage of glycerin, such as cements 7 (14 min) and 8 (25 min). These numbers are associated with solutions containing the maximum and minimum percentage of glycerin together with the upper limit of chitosan. The cements had an intermediate setting time at the lower limit of chitosan. Glycerin is a highly water-soluble polymer; thus, it can form three-dimensional network structures and entangles the powder phase of the cements, obtaining greater dimensional stability and working time [23].

The F value was used in ANOVA analysis to determine the ratio of explained variance to unexplained variance. For the model to predict the behavior of the variable, the value of the $F_{calculated}$ must be greater than the $F_{tabulated}$, which implies that the R^2 is only statistically valid if this requirement is met. For the L/P response, the $F_{calculated}$ value (3.99) was lower than the $F_{tabulated}$ value (6.16), indicating that the linear model could not explain the behavior of the response, requiring the application of another type of model. The same was observed for the ANOVA analysis of the ST, which showed a $F_{calculated}$ value (4.13) lower than the $F_{tabulated}$ (6.16).

Therefore, it was impossible to determine an equation describing the model or build a response surface curve for the L/P and ST.

The maximum hydration temperature of the cements ranged from 36.6 to 45.6 ºC, which is considerably lower than the temperatures reached using PMMA cements (66 to 120 ºC) [2]. This is an important achievement that allows potentially overcoming one of the well-known, traditional drawbacks associated with using PMMA cement, i.e. the risk of thermal damage to healthy tissue (necrosis). The analysis of the effects showed that the variables "glycerin", "S_3A", "S_3A and glycerin" and "chitosan and glycerin" were statistically significant over the response. The Pareto chart of standardized effects (Figure 7) confirmed these results.

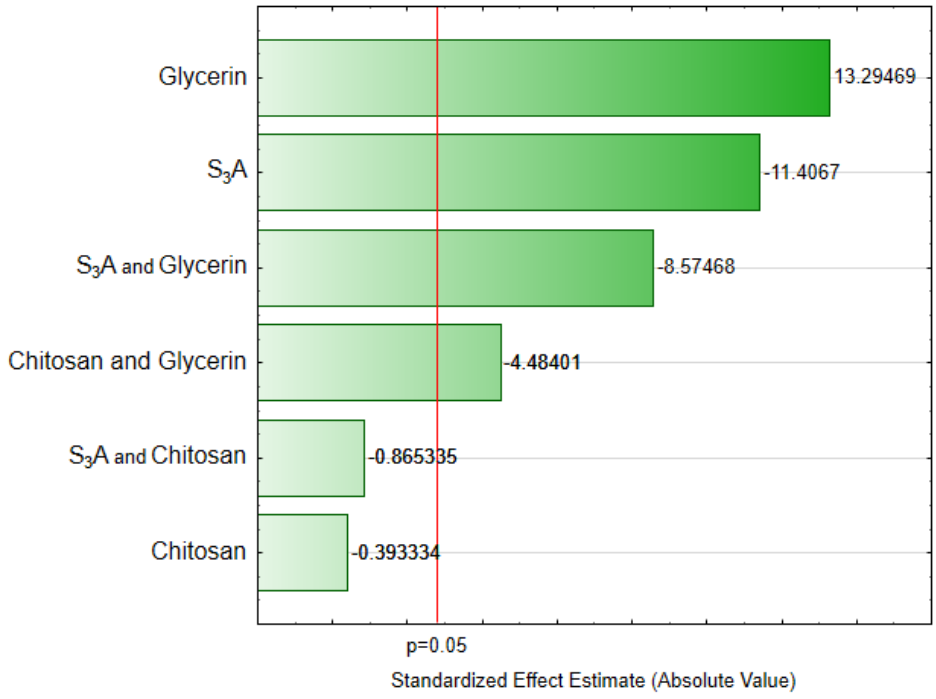


Figure 7. Pareto chart for maximum hydration temperature response (T_{max}). 2^3 design refers to the type of experimental planning adopted. 2 corresponds to the levels (+ and -) and, 3 to the process input variables (X1, X2 and X3) (Table 1). Mean square residual = 0.2019886.

The response surface graph (Figure 8) shows that T_{max} increases by using more glycerin in the liquid phase of the cements. For example, T_{max} reaches 45.6 ºC in the case of cement 5. Glycerin not only allows better handling of cements [48] but can also be indicated as an adjuvant for the hydration reaction [23]. At first, when using only the chitosan solution without the addition of glycerin, it was not possible to hydrate the cements as phase separation occurred.

The addition of glycerin into the chitosan solution caused the exothermic reaction of hydration of the cements as it acted as a coupling agent between the organic and inorganic phases.

The response surface graph displayed in Figure 6 also shows that a higher amount of S_3A diminishes the T_{max}, as observed with cement 2 (36.6 ºC). This can be explained by the fact that a higher percentage of S_3A implies a lower portion of $C_{12}A_7$, which, in turn, contains a high content of CaO, making the cement more reactive, causing faster and more intense hydration [10] and consequently increasing the T_{max}.

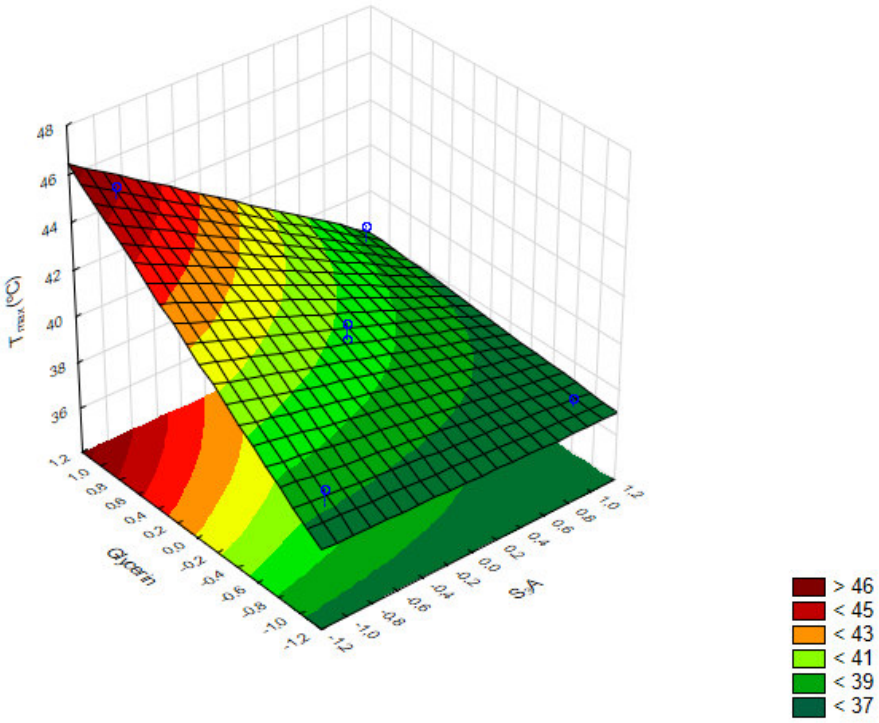


Figure 8. Response surface graph for the maximum temperature of hydration (T_{max}) concerning the amount of S_3A in the solid phase of the cements, and glycerin in the liquid phase.

As for the interaction of the variables "S_3A and glycerin", the lowest T_{max} was obtained for the cement prepared from the upper limit of S_3A and the lower limit of glycerin.

As regards the interaction of the variables "chitosan and glycerin" (Figure 9), the cement with the lowest T_{max} was made when the solution was prepared from the lower limits of both chitosan and glycerin.

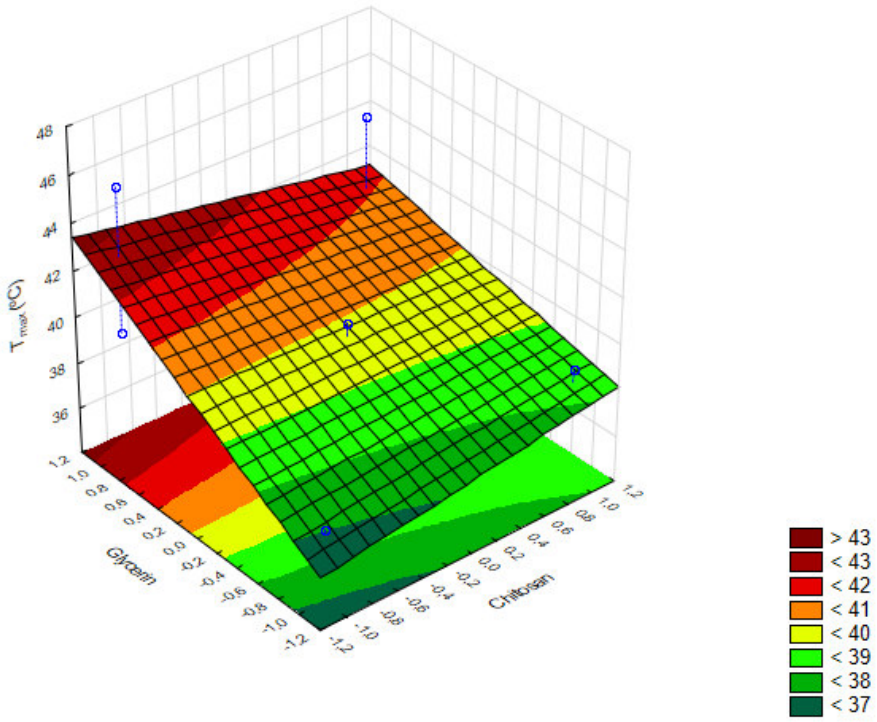


Figure 9. Response surface graph for the maximum hydration temperature (T_{max}) considering the amount of chitosan and glycerin in the liquid phase of cements.

Through ANOVA analysis, it was found that the $F_{calculated}$ value (122.51) of the model was considerably higher than the $F_{tabulated}$ value (6.16), suggesting that the model is statistically significant and predictive. The model exhibited a coefficient of determination (R^2) of 98.79%, an adjusted coefficient of determination (R^2aj) of 97.98%, and an ability to predict new values of 96.58%. Equation (4) shows the model.

$$T_{max} = 39.74 - 1.81X_1 + 2.11X_3 - 1.36X_1X_3 - 0.71X_2X_3 \quad (4)$$

3.2.2. Compressive Strength

Table 4 shows the average compressive strength of all compositions, ranging from 1.36 to 4.61 MPa. Most of these values can be considered acceptable for osseous applications as they fall in the typical ranges assessed for human trabecular bone. In fact, although the mechanical performance of bone depends on the harvesting site as well as patient's age, sex and clinical conditions, some "general" reference ranges for compressive strength have been reported in the literature, for example, 1-16 MPa [49], 1.5-7.5 MPa [50] and 2-12 MPa [51].

Table 4. Average compressive strength of all cements.

Cements	Compressive strength (MPa)
1	4.61
2	1.36
3	1.50
4	1.52
5	4.18
6	1.81
7	3.13
8	3.35
9	2.12
10	2.35
11	1.86

Through the analysis of the effects, it was found that only the terms "S_3A and chitosan" and "S_3A", with p-values of 1.2 and 1.6%, respectively, were statistically significant and corroborated by the Pareto chart (Figure 10).

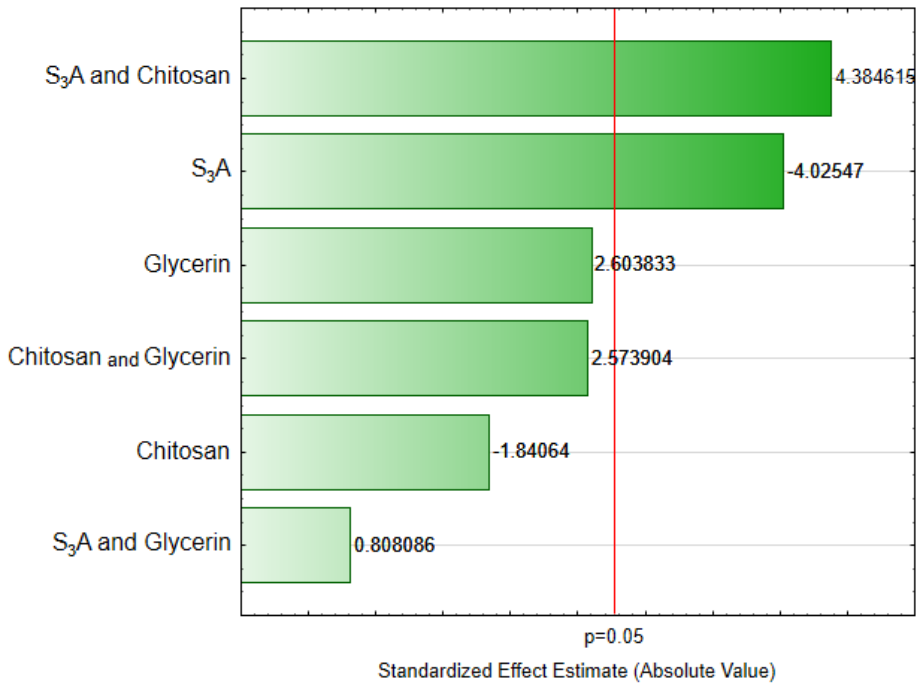


Figure 10. Pareto chart for average compressive strength. 2^3 design refers to the type of experimental planning adopted. 2 corresponds to the levels (+ and -) and, 3 to the process input variables (X1, X2 and X3) (Table 1). Mean square residual = 0.2232761.

The response surface graph (Figure 11) demonstrates that using a lower amount of S_3A promotes the increment of strength. The greatest response is obtained when the cement formulations contain the lowest limit of S_3A and chitosan, as shown for cement 1 that has a strength of 4.61 MPa. A lower amount of S_3A in the cement formulation means a higher amount of $C_{12}A_7$. Cements with high calcium content, e.g., in the case of $C_{12}A_7$-rich compositions, set and cure faster, thus inhibiting the materials from acquiring higher levels of mechanical strength. This is due to the reactivity of CaO which, when hydrated, promotes the formation of less soluble hydrated salts. In this way, the precipitation of these hydrated compounds occurs in an accelerated way [52, 53].

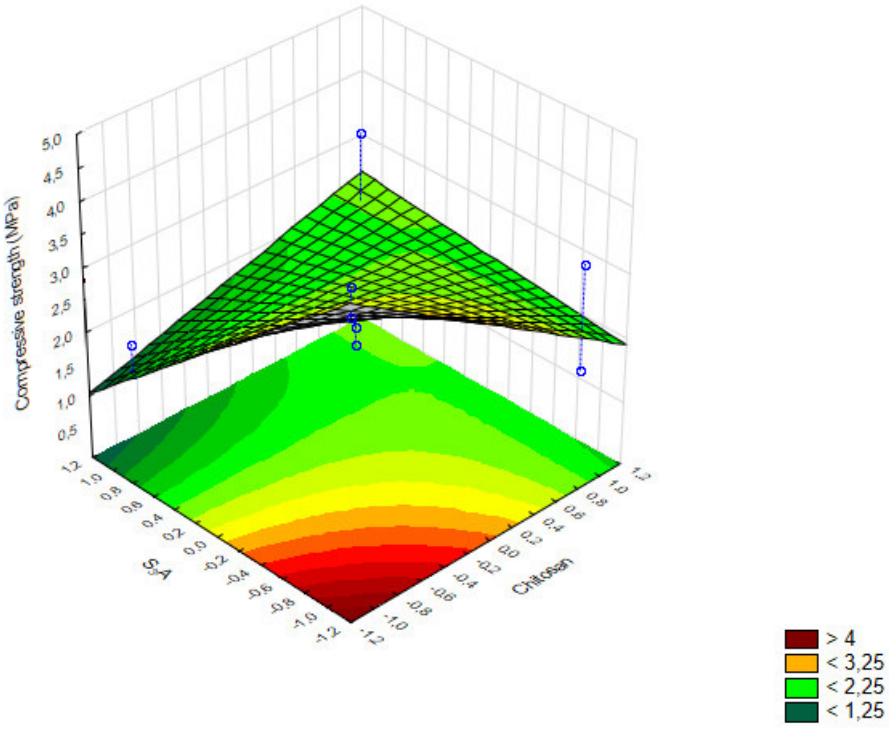


Figure 11. Response surface graph for the compressive strength of cements as a function of S_3A content in the powder phase and chitosan in the liquid phase.

The use of chitosan in the liquid phase of cements has been reported to improve cohesion as well as mechanical and biological responses [54]. In this study, the "glycerin" and "chitosan and glycerin" effects were not statistically significant (p-value of 6 and 6.2%, respectively). But, the response surface graph displayed in Figure 12 shows that increasing chitosan content tends to decrease the strength because of the incompatibility between the organic phases and inorganic compounds that make up the cements, which justifies the use of glycerin as a coupling

agent. It is possible to obtain higher compressive strength using the upper limit of chitosan, provided that the percentage of glycerin is simultaneously increased.

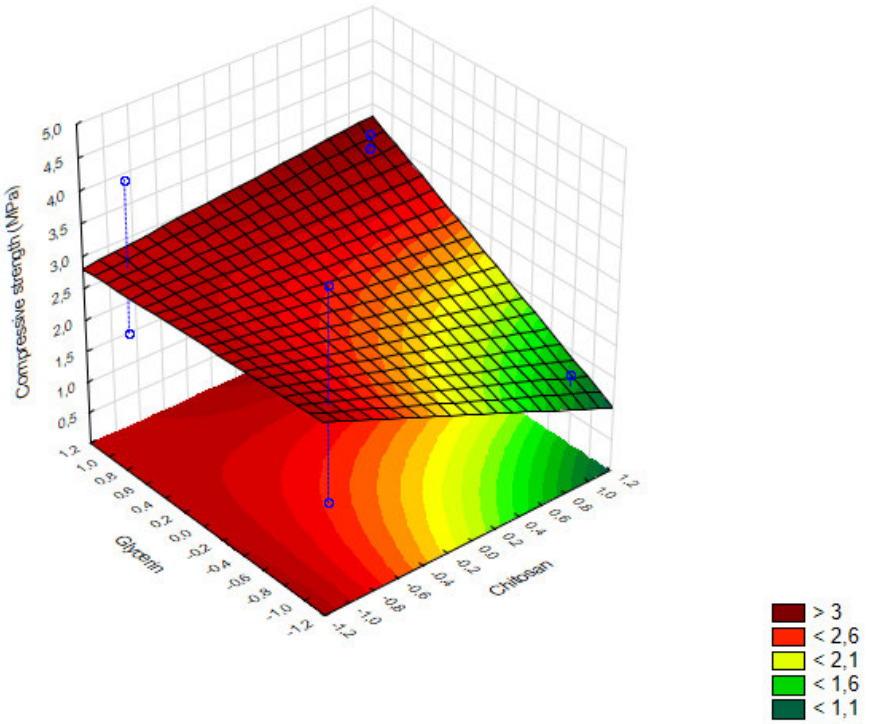


Figure 12. Response surface graph for the compressive strength of cements as a function of the amount of chitosan and glycerin in the liquid phase.

The ANOVA analysis showed that the $F_{calculated}$ value (9.11) of the model was 1.48 times greater than the $F_{tabulated}$ value (6.16), signifying that the model is adjusted and statistically significant. However, it is not predictive. The model exhibited an R^2 of 85.86%, R^2aj of 76.44% and an ability to predict new values of only 39.55%. Equation (5) shows the model.

$$Compressive\ strength\ = 2.53 - 0.67X_1 + 0.43X_3 + 0.73X_1X_2 + 0.43X_2X_3 \qquad (5)$$

3.2.3. Radiopacity

Figure 13 shows the digital radiographic images of 3 samples for each of the 11 compositions, along with the aluminum scale. The aluminum scale appears from the first to the eighth step on the right side of each image, with the darkest gray tone corresponding to 1 mm thickness and the lightest to 8 mm.

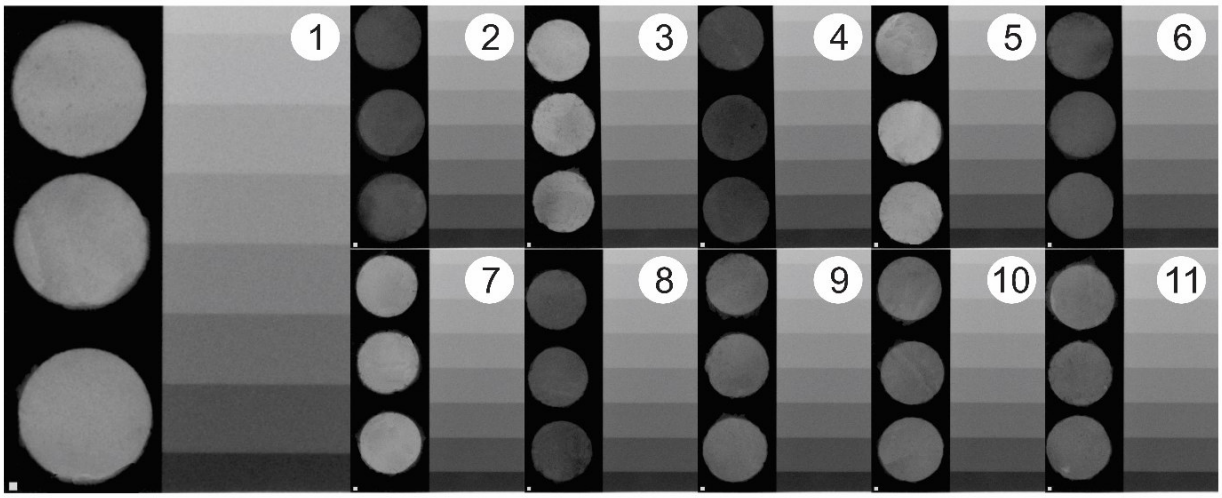


Figure 13. Radiographic images of 3 samples of each composition.

A calibration curve was drawn to calculate the radiopacity of each sample. Figure 14 shows the fitted line to data points of "aluminum scale thickness (mm Al)" vs. "average gray level" as well as the model equation (mm Al = -2.882+0.05579×(average level of gray)), the standard deviation of 0.299173, R^2 of 98.7% and R^2aj of 98.5%.

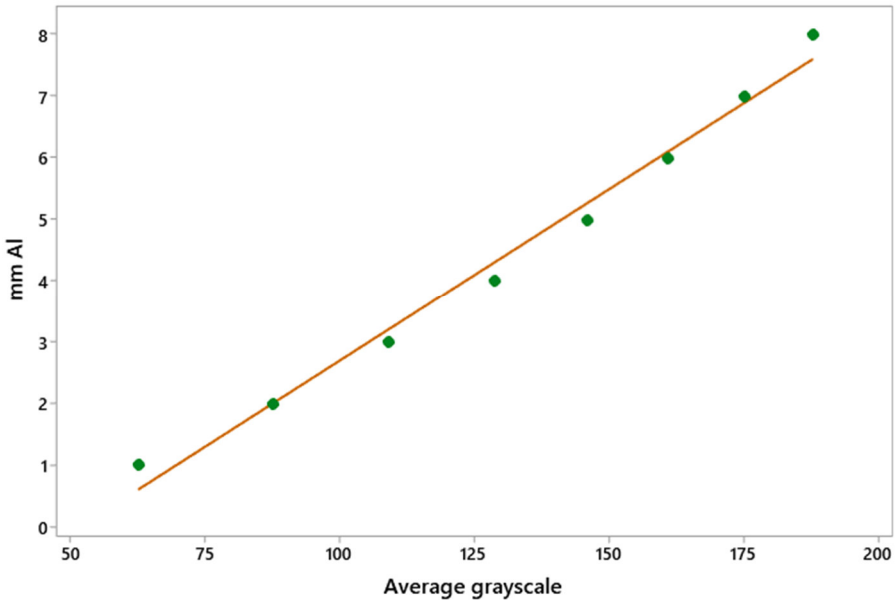


Figure 14. The calibration curve for "aluminum scale thickness (mm Al)" vs. "average gray level" of radiographic images.

The radiopacity of each cement obtained from the calibration curve is listed in Table 5 together with the coefficients of variation (CV) from the averages.

Table 5. Average values of radiopacity in mm Al for each composition.

Cements	Radiopacity (mm Al)	CV (%)
1	1.81	0.05
2	4.93	0.07
3	1.39	0.19
4	5.05	0.18
5	2.06	0.12
6	5.41	0.06
7	1.76	0.04
8	5.02	0.19
9	2.81	0.03
10	2.87	0.07
11	2.78	0.13

Cements 2, 4, 6 and 8 showed excellent radiopacity, that is, greater than that of 3 mm Al. Cements 9, 10 and 11 presented radiopacity close to 3 mm Al. The analysis of effects revealed that, as expected, only the "S_3A" variable, with a p-value of 0.1%, had a statistically significant influence on the "radiopacity" response. The Pareto chart of standardized effects (Figure 15) corroborated this finding.

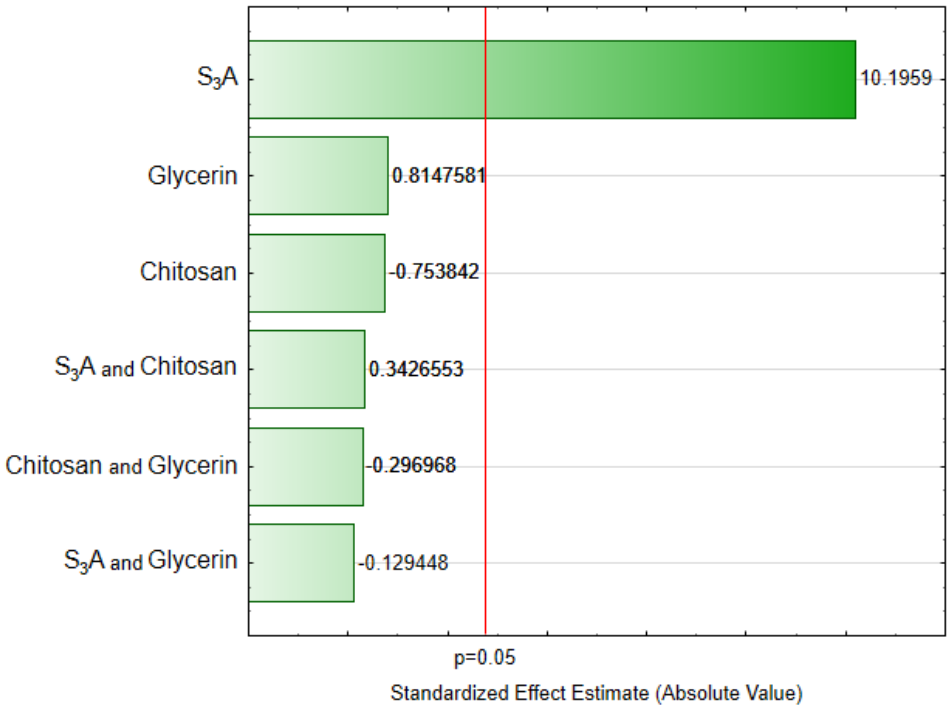


Figure 15. Pareto chart of all standardized effects on the radiopacity response. 2^3 design refers to the type of experimental planning adopted. 2 corresponds to the levels (+ and -) and, 3 to the process input variables (X1, X2 and X3) (Table 1). Mean square residual = 0.2155858.

The response surface graph displayed in Figure 16 clearly shows that the higher percentage of S_3A makes cements more radiopaque. Cements 2, 4, 6 and 8 showed radiopacity of 4.94, 5.05, 5.41 and 5.02 mm Al, respectively. These cements have 80 wt.% of S_3A in their solid phases. However, the S_3A powder used in the preparation of cements is not 100% pure, there is a fraction of SA and $SrCO_3$ (Figure 1). It was possible to obtain radiopaque cements, but they could be even more radiopaque if it were possible to obtain a pure S_3A phase. Still, the results obtained for the radiopacity of the cements in this study were better than those obtained by Barbosa *et al.* [41], considering the same fraction (80 wt.%) of S_3A. This variation could be due to the difference between the particle size of the S_3A used in this study (d_{50}=13.7 μm) and Barbosa *et al.* [41] (d_{50}=3.1 μm). Results found by Saghiri *et al.* [55] showed that cements containing radiopacifying particles with a size of 10 μm showed greater radiopacity than cements containing nanoscale particles of the same agent. According to them, the smaller the size of the particles, the greater tendency to agglomeration. If the radiopacifying agent is not homogeneously dispersed in the cement, its ability to block X-rays is compromised, making the material less radiopaque.

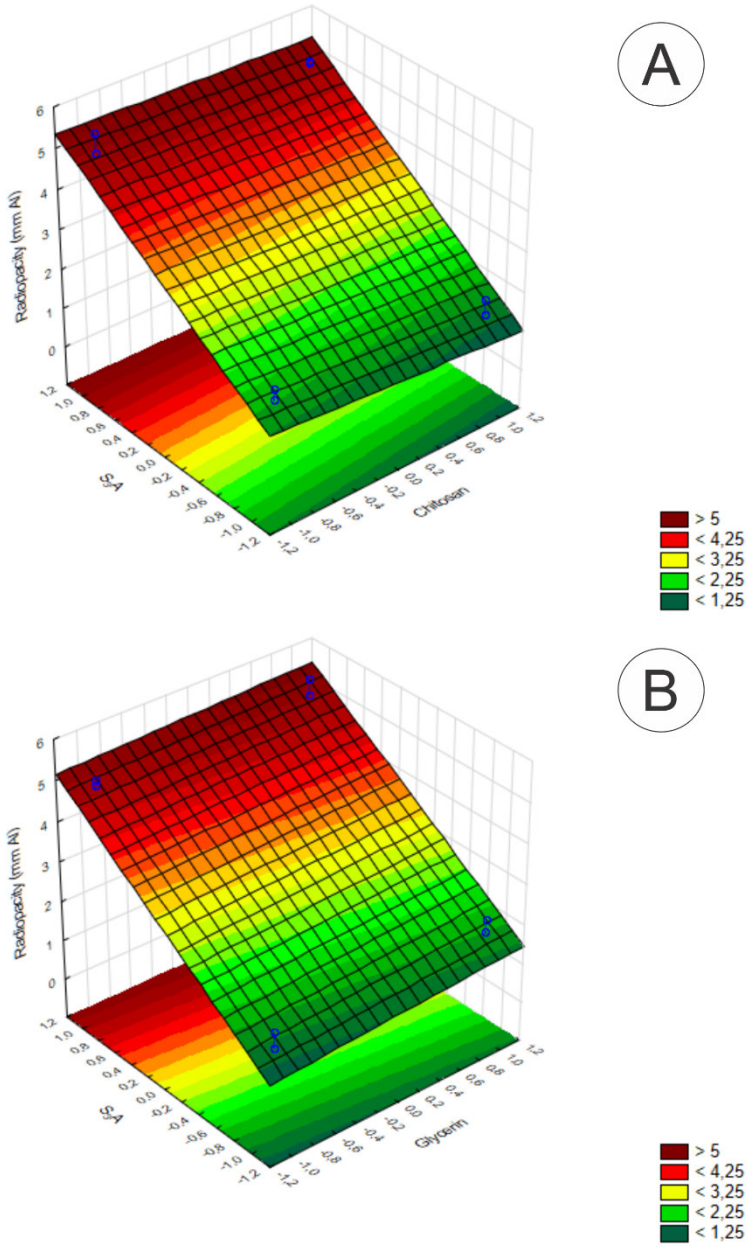


Figure 16. (A) Response surface plot of S_3A and chitosan on radiopacity; (B) Response surface graph of S_3A and glycerin on radiopacity.

Through the ANOVA analysis, it was observed that the $F_{calculated}$ (171.53) of the model was substantially higher than the $F_{tabulated}$ (6.16), indicating that the model is significant and predictive. The model had an R^2 of 95.01%, R^2aj of 94.46%, and an ability to predict new values of 92.94%. Equation (6) expresses the model:

$$Radiopacity = 3.263 + 1.674X_1 \quad (6)$$

3.3. Characterization of optimized cement

The statistical analysis of the results obtained in the characterization of cements enabled the determination of a specific composition that could exhibit a T_{max} as close as possible to 37 ºC, reach a compressive strength of at least 7 MPa (i.e., the mid-value range of human trabecular bone according to Hench [51]) and have a radiopacity above 3 mm Al. The composition was: 60 wt.% S_3A + 40 wt.% $C_{12}A_7$ (solid phase); 2 wt.% chitosan dissolved in acetic acid solution at 1 v/v%, with 30:1 addition of glycerin, relative to the amount of chitosan.

3.3.1. Evaluation of the phases

Figure 17 shows the XRD pattern obtained for the cement of optimized composition. In addition to the $C_{12}A_7$, C_3A, S_3A, SA and $SrCO_3$ phases, present in the raw materials for the preparation of the cements (Figure 1), two new phases were identified: tristrontium aluminate hexahydrate ($3SrO.Al_2O_3.6H_2O$, S_3AH_6) (according to ICSD 00–024–1186) with low intensity peaks at 30.72º and 50.22º and the high alumina gel phase ($Al(OH)_3$, AH_3) (ICSD 00–029–0041) with a peak at 44.08 º. These phases are hydrates. Comparing the diffraction pattern of cement with that of ceramic powders (Figure 1), it is noted that the intensities of the peaks referring to the S_3A and SA significantly reduced. According to Ptáček et al. [35], hydration of strontium aluminate cements begins immediately after mixing with water, with no induction period being observed. Thus, the S_3AH_6 and AH_3 phases form rapidly and consist of the main hydration products of these cements, which explains the rapid decline in the intensity of the S_3A and SA peaks. It is also possible to observe that the main peaks referring to $SrCO_3$ (25.18º and 27.77º) became more intense after hydration, this is due to the presence of atmospheric CO_2 that, when reacting with the hydrate S_3AH_6, forms $SrCO_3$ [41]. It is also noted that, although the diffraction pattern does not show peaks referring to the polymeric phase of the cement (chitosan hydration solution with glycerin), the base of the crystallographic profile exhibits amorphous behavior when compared to the diffraction patterns of ceramic powders before hydration (Figure 1), an indication for the presence of the polymeric phases [56].

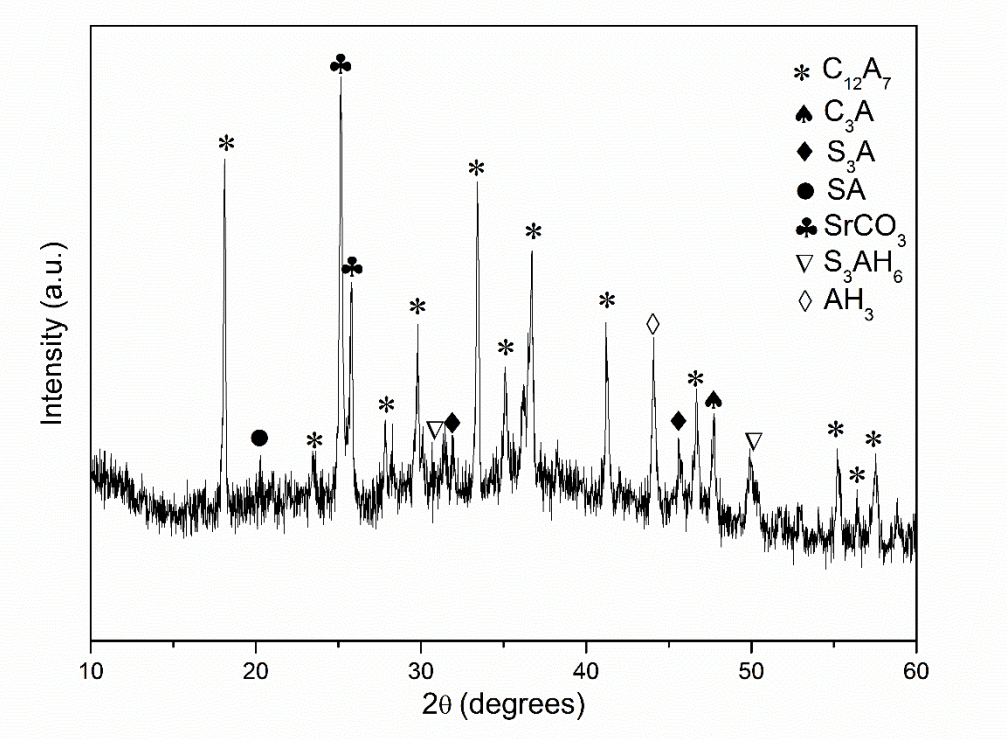


Figure 17. XRD pattern of cement with optimized composition after 24 h of hydration.

3.3.2. Evaluation of chemical groups

The FTIR spectrum obtained for the cement (Figure 18) shows, in the region of 3750 – 3000 cm^{-1}, the formation of a broad band of low intensity caused by the stretching of the -OH groups in the adsorbed water molecules and polymers such as chitosan [57] and glycerin [58]. In addition to the stretching band of the -OH groups, the stretching of the -NH groups of chitosan also occurs [57]. In the region of 3000–2700 cm^{-1}, an absorption band forms by the junction of two low-intensity peaks, attributed to the symmetrical and asymmetrical stretching vibrations of the -CH group. This band is also characteristic in the chitosan [59] and glycerin [58] spectra. The narrow, low-intensity peak at 1745 cm^{-1} is caused by the doubling of the -OH groups in the adsorbed water molecules (Ptáček et al., 2014). Between 1550–1290 cm^{-1}, the peak centered at 1455 cm^{-1} is caused by the vibrations of CO_3^{-2}, characteristic of $SrCO_3$ [35, 60]. In the region between 1170-970 cm^{-1}, the peak centered at 1070 cm^{-1} results from the asymmetric stretching of C–O–C bonds. This peak can be observed in the same way in the spectra obtained for chitosan [61] and glycerin [58]. The vibrations comprising the regions of 900–700 cm^{-1} and 680–500 cm^{-1} are attributed to asymmetric bending of Al–O–Al in tetrahedral and octahedral coordination, respectively. This type of vibration is characteristic of aluminates

[62], with the peak at 855 cm^{-1} corresponding to the SA phase and the peak at 560 cm^{-1} referring to the hydrate S_3AH_6 [35].

It was impossible to identify the main, well-defined peak corresponding to the S_3AH_6 hydrate, which occurs at 3664 cm^{-1}, or AH_3 peaks. However, according to Ptáček et al. [35], the definition of hydrate peaks increases with the passage of hydration time. Overall, the results obtained in the evaluation of the chemical groups of the cement through the FTIR corroborate the phase evaluation by XRD.

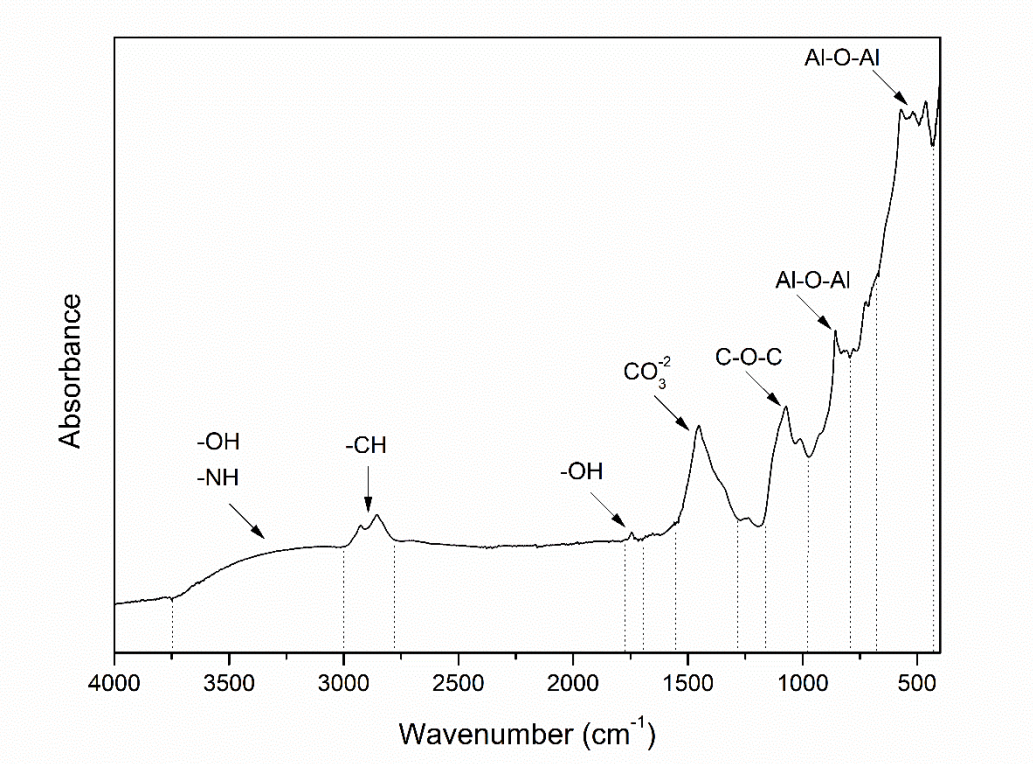


Figure 18. FTIR of cement with optimized composition after 24 h of hydration.

3.3.3. Microstructural evaluation

Figure 19 shows the micrograph of the morphology of the cement of optimized composition. The presence of micropores throughout the sample is evident, caused by excessive hydration by solution and/or intergranular spaces [63]. It is known that the presence of micro and macropores are of paramount importance for the biological properties of cements [64], but they can also act as stress concentrators, causing a reduction in the mechanical properties of the material [65].

Bright agglomerates formed by submicron particles can be observed in the micrograph on the surface of the sample; the literature suggests that these bright agglomerates could be attributed to the hydrate S_3AH_6 [33] while the darker agglomerates, present in a smaller proportion, could correspond to the hydrate AH_3 [41]. The results obtained in the morphological analysis regarding the formation of hydrates corroborate the results found in the evaluation of the phases and chemical groups of the cement (Figures 17 and 18).

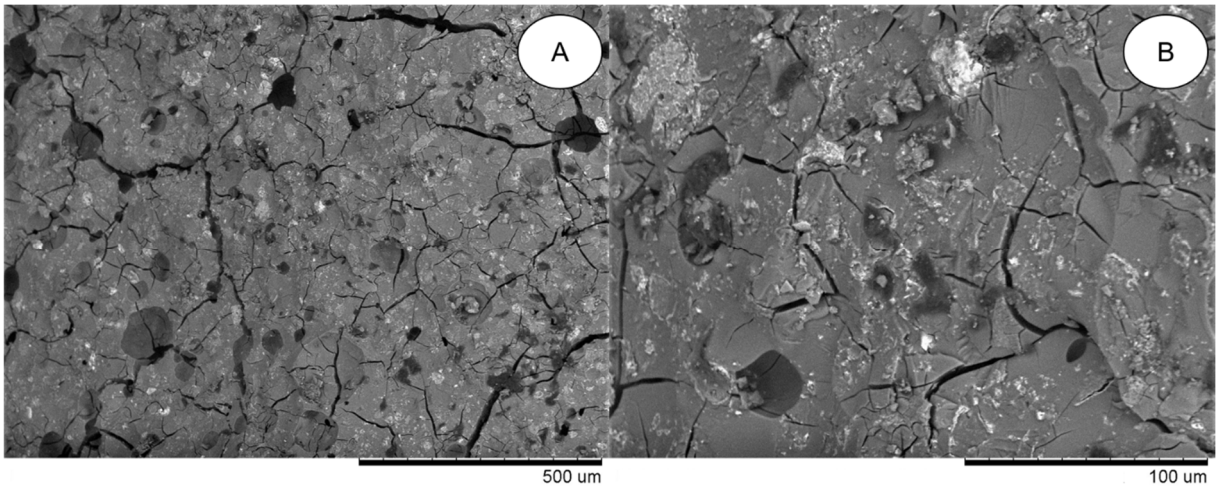


Figure 19. SEM micrograph of the optimized composition cement after 24 h of hydration at ×200 (A) and ×1000 (B).

3.3.4. Validation of equations

In order to validate the equations found for T_{max} (Equation 4), compressive strength (Equation 5) and radiopacity (Equation 6), 3 samples of this optimized cement with L/P of 1.5 ml/g were prepared and analyzed for each test (T_{max}, compressive strength and radiopacity). It is worth noting that the variables X1, X2 and X3, from Equations 4, 5 and 6, are coded values as shown in Table 1. Therefore, before applying these equations, it is necessary to code the actual values of the amounts of S_3A, chitosan and glycerin which are x1=60, x2=2 and x3=30, respectively. To achieve this, Equations (7), (8) and (9) were used.

$$X1 = \frac{x1 - 50}{30} \quad (7)$$

$$X2 = \frac{x2 - 1}{0.5} \quad (8)$$

$$X3 = \frac{x3 - 10}{5} \quad (9)$$

Table 6 displays the expected values for T_{max}, compressive strength and radiopacity through the application of Equations 4, 5 and 6, respectively, and the average of the values measured from the experiments.

Table 6. Expected values and measured values for the maximum temperature (T_{max}) compressive strength and radiopacity of the testing samples.

Values	T_{max} (ºC)	Compressive strength (MPa)	Radiopacity (mm Al)
Expected	40.08 ± 0.41	7.95 ± 0.55	3.82 ± 0.36
Measured	40.34 ± 1.82	7.75 ± 0.55	3.76 ± 0.14

The objectives required with the specific composition of the cements were achieved. We can notice that the values found were very close to the values predicted by the equations, even for the result of the compressive strength analysis, whose equation has a predictive capacity of only 39.55%. This indicates the robustness of the model adopted and the precision of the equations obtained. The reliability of the model could be further increased by testing a larger number of samples.

For comparison, Table 7 shows the literature data on T_{max}, compressive strength and radiopacity of some ceramic cements for biomedical applications whose base composition contains calcium and/or strontium. The composition-optimized cement obtained in this study seems to stand out for its T_{max} and radiopacity. As for its compressive strength (7.75 MPa), it is in the middle-value range for trabecular bone, according to Hench [51]. However, Table 7 shows that the cements that presented the highest compressive strength were placed in saturated environments (100% humidity at 37 ºC) or immersed in simulated body fluid (SBF) at 37 ºC for at least 24 h, before being evaluated, which favors the formation of hydrates, contributing to greater strength.

Table 7. Some results for T_{max}, compressive strength and radiopacity of ceramic cements reported in the literature.

Cement composition	T_{max} (ºC)	Compressive strength (MPa)	Radiopacity (mm Al)	Reference
Based on calcium aluminate	-	67 ± 1.8 (after 7 days in contact with SBF at 37 ºC)	< 1	[6]
LiCl–containing calcium aluminate	58.1–60.3	95–105 (after 24 h of immersion in SBF at 37 ºC)	-	[66]
Sr–modified premixed calcium phosphate	-	21.6	2.01	[67]
Based on Ca- and Sr-aluminates	33.5	5.1	3.1	[41]
Sr-doped hydroxyapatite	-	73.4 (after 23 h incubated in humidity of 100% at 37 ºC)	Tested qualitatively	[68]

4. Conclusions

Ceramic powders composed of $C_{12}A_7$ and S_3A obtained via SCS and chitosan solution with glycerin (liquid phase) were used to develop a new bone cement. The 2^k factorial experimental design was applied to optimize the maximum temperature of hydration (T_{max}), compressive strength, and radiopacity of the cement. The application of models obtained by the optimization process allowed the determination of a specific composition for the cement (60 wt.% S_3A + 40 wt.% $C_{12}A_7$ (solid phase), 2 wt.% chitosan dissolved in acetic acid solution at 1% v/v, with the addition of 30:1 of glycerin, which, in turn, provided the desired values for properties). The cements with this composition had an average T_{max} of 40.34 ºC, compressive strength of 7.75 MPa and radiopacity of 3.76 mm Al. In short, the methodology resulted in a relatively simple and efficient mathematical model to predict the behavior of cements based on S_3A, $C_{12}A_7$, chitosan and glycerin. This approach is a valuable tool to tailor the structural (compressive strength) and functional properties (T_{max} and radiopacity) of cements to meet the required needs. It can be potentially extended to a wide range of bioceramics and biomaterials in general. Applying such an approach to study, design and finely tune the biological properties of cements will be the future step of this research.

References

[1] GINEBRA, M.-P.; MONTUFAR, E. B. Bone rapair biomaterials. Cements as bone repair materials. Second edition. Elsevier Ltd, 2019,p. 233-271.

[2] DEB, S.; KOLLER, G. Acrylic bone cement: Genesis and evolution. **Orthopaedic Bone Cements**, p. 167–182, 2008.

[3] VAISHYA, R.; CHAUHAN, M.; VAISH, A. Bone cement. **Journal of Clinical Orthopaedics and Trauma**, v. 4, n. 4, p. 157–163, 2013.

[4] LEWIS, G. Injectable bone cements for use in vertebroplasty and kyphoplasty: State-of-the-art review. **Journal of Biomedical Materials Research - Part B Applied Biomaterials**, v. 76, n. 2, p. 456–468, 2006.

[5] OLIVEIRA, I. R. et al. Surface properties of calcium aluminate cement blends for bone repair applications. **Ceramics International**, v. 46, n. 9, p. 14241–14251, 2020.

[6] PARREIRA, R. M. et al. Calcium aluminate cement-based compositions for biomaterial applications. **Ceramics International**, v. 42, n. 10, p. 11732–11738, 2016.

[7] WOODARD, J. R. et al. The mechanical properties and osteoconductivity of hydroxyapatite bone scaffolds with multi-scale porosity. **Biomaterials**, v. 28, n. 1, p. 45–54, 2007.

[8] MA, H. et al. 3D-printed bioceramic scaffolds: From bone tissue engineering to tumor therapy. **Acta Biomaterialia**, v. 79, p. 37–59, 2018.

[9] LÖÖF, J. **Calcium-Aluminate as Biomaterial**: synthesis, design and evaluation. Acta. Univ. Upsal., p. 15, 2008.

[10] ANDRADE, T. L. et al. Otimização da síntese das fases de cimento de aluminato de cálcio para fins biomédicos. **Ceramica**, v. 60, n. 353, p. 88–95, 2014.

[11] TANAKA, Y.; YAMASHITA, K. Bioceramics and their clinical applications. **Fabrication processes for bioceramics**. Woodhead Publishing Limited, 2008, p. 28-52.

[12] SHEPHERD, J. H.; SHEPHERD, D. V.; BEST, S. M. Substituted hydroxyapatites for bone repair. **Journal of Materials Science: Materials in Medicine**, v. 23, n. 10, p. 2335–2347, 2012.

[13] KAYGILI, O.; TATAR, C.; YAKUPHANOGLU, F. Structural and dielectrical properties of Mg 3-Ca 3(PO 4) 2 bioceramics obtained from hydroxyapatite by sol-gel method. **Ceramics International**, v. 38, n. 7, p. 5713–5722, 2012.

[14] LIN, K. et al. Strontium substituted hydroxyapatite porous microspheres: Surfactant-free hydrothermal synthesis, enhanced biological response and sustained drug release. **Chemical Engineering Journal**, v. 222, p. 49–59, 2013.

[15] KAVITHA, M. et al. Optimization of process parameters for solution combustion synthesis of Strontium substituted Hydroxyapatite nanocrystals using Design of Experiments approach. **Powder Technology**, v. 271, p. 167–181, 2015.

[16] DEGANELLO, F.; MARCÌ, G.; DEGANELLO, G. Citrate-nitrate auto-combustion synthesis of perovskite-type nanopowders: A systematic approach. **Journal of the European Ceramic Society**, v. 29, n. 3, p. 439–450, 2009.

[17] DEGANELLO, F.; TYAGI, A. K. Solution combustion synthesis, energy and environment: Best parameters for better materials. **Progress in Crystal Growth and Characterization of Materials**, v. 64, n. 2, p. 23–61, 2018.

[18] NOVIKOV, V. et al. Solution Combustion Synthesis of nanoscale Cu-Cr-O spinels: Mechanism, properties and catalytic activity in CO oxidation. **Ceramics International**, v. 43, n. 15, p. 11733–11742, 2017.

[19] ZHANG, Y.; STANGLE, G. C. Preparation of fine multicomponent oxide ceramic powder by a combustion synthesis process. **Journal of Materials Research**, v. 9, n. 8, p. 1997–2004, 1994.

[20] CZECHOWSKA, J. et al. The importance of chitosan and nano-TiHA in cement-type composites on the basis of calcium sulfate. **Ceramics International**, v. 42, n. 14, p. 15559–15567, 2016.

[21] SHI, Z. et al. Antibacterial and mechanical properties of bone cement impregnated with chitosan nanoparticles. **Biomaterials**, v. 27, n. 11, p. 2440–2449, 2006.

[22] TAKAGI, S. et al. Premixed Calcium-Phosphate Cement Pastes. **Journal of Biomedical Materials Research - Part B Applied Biomaterials**, v. 67, n. 2, p. 689–696, 2003.

[23] WANG, X.; YE, J.; WANG, H. Effects of additives on the rheological properties and injectability of a calcium phosphate bone substitute material. **Journal of Biomedical Materials Research - Part B Applied Biomaterials**, v. 78, n. 2, p. 259–264, 2006.

[24] CAREY, L. E. et al. Premixed rapid-setting calcium phosphate composites for bone repair. **Biomaterials**, v. 26, n. 24, p. 5002–5014, 2005.

[25] XU, H. H. K. et al. Premixed calcium phosphate cements: Synthesis, physical properties, and cell cytotoxicity. **Dental Materials**, v. 23, n. 4, p. 433–441, 2007.

[26] SHOJAEE KANG SOFLA, M.; MORTAZAVI, S.; SEYFI, J. Preparation and characterization of polyvinyl alcohol/chitosan blends plasticized and compatibilized by glycerol/polyethylene glycol. **Carbohydrate Polymers**, v. 232, n. November 2019, 2020.

[27] ANTONIJEVIĆ, D. et al. Influence of the addition of different radiopacifiers and bioactive nano-hydroxyapatite on physicochemical and biological properties of calcium silicate based endodontic ceramic. **Ceramics International**, v. 47, n. 20, p. 28913–28923, 2021.

[28] QUEIROZ, M. B. et al. Physicochemical, biological, and antibacterial evaluation of tricalcium silicate-based reparative cements with different radiopacifiers. **Dental Materials**, v. 37, n. 2, p. 311–320, 2021.

[29] LIU, H. et al. Enhancing effects of radiopaque agent BaSO4 on mechanical and biocompatibility properties of injectable calcium phosphate composite cement. **Materials Science and Engineering C**, v. 116, n. 8, p. 110904, 2020.

[30] PRENTICE, L. H.; TYAS, M. J.; BURROW, M. F. The effect of ytterbium fluoride and barium sulphate nanoparticles on the reactivity and strength of a glass-ionomer cement. **Dental Materials**, v. 22, n. 8, p. 746–751, 2006.

[31] BOSSO-MARTELO, R. et al. Physicochemical properties of calcium silicate cements associated with microparticulate and nanoparticulate radiopacifiers. **Clinical Oral Investigations**, v. 20, n. 1, p. 83–90, 2016.

[32] SNEHA, K. R.; SAILAJA, G. S. Intrinsically radiopaque biomaterial assortments: A short

review on the physical principles, X-ray imageability, and state-of-the-art developments. **Journal of Materials Chemistry B**, v. 9, n. 41, p. 8569–8593, 2021.

[33] BARBOSA, W. T. et al. Combustion synthesis and characterization of Sr3Al2O6. **International Journal of Applied Ceramic Technology**, v. 16, n. 2, p. 595–601, 2019a.

[34] CHATTERJEE, A. K. Re-examining the prospects of aluminous cements based on alkali-earth and rare-earth oxides. **Cement and Concrete Research**, v. 39, n. 11, p. 981–988, 2009.

[35] PTÁČEK, P. et al. Synthesis, hydration and thermal stability of hydrates in strontium-aluminate cement. **Ceramics International**, v. 40, n. 7 PART A, p. 9971–9979, 2014.

[36] MONTGOMERY, D. C. Design and analysis of experiments. Ninth edition. Hoboken, NJ: John Wiley& Sons,2017. ISBN 1119113474.

[37] RODRÍGUEZ, M. A.; AGUILAR, C. L.; AGHAYAN, M. A. Solution combustion synthesis and sintering behavior of CaAl 2O4. **Ceramics International**, v. 38, n. 1, p. 395–399, 2012.

[38] International Organization for Standardization, ISO DIS 18531:2015 – Implants for surgery, (2015).

[39] Associação Brasileira de Normas Técnicas, ABNT NBR ISO 5833:2004 – Implants for surgery – Acrylic resin cements, (2004).

[40] Associação Brasileira de Normas Técnicas, ABNT NBR ISO 13116:2020 – Dentistry – Test method for determining radio-opacity of material, (2020).

[41] BARBOSA, W. T. et al. New cement based on calcium and strontium aluminates for endodontics. **Ceramics International**, v. 45, n. 16, p. 19784–19792, 2019b.

[42] MEZA-TRUJILLO, I.; DEVRED, F.; GAIGNEAUX, E. M. Production of high surface area mayenite (C12A7) via an assisted solution combustion synthesis (SCS) toward catalytic soot oxidation. **Materials Research Bulletin**, v. 119, n. July, p. 110542, 2019.

[43] ROJAS-HERNANDEZ, R. E.; RODRIGUEZ, M. A.; FERNANDEZ, J. F. Role of the oxidizing agent to complete the synthesis of strontium aluminate based phosphors by the combustion method. **RSC Advances**, v. 5, n. 4, p. 3104–3112, 2015.

[44] CAO, Z. et al. One pot solution combustion synthesis of highly mesoporous hematite for photocatalysis. **Ceramics International**, v. 41, n. 2, p. 2806–2812, 2015.

[45] NOVITSKAYA, E. et al. A review of solution combustion synthesis: an analysis of parameters controlling powder characteristics. **International Materials Reviews**, 2020.

[46] OLIVEIRA, I. R.; ORTEGA, F. S.; PANDOLFELLI, V. C. Hydration of CAC cement in a castable refractory matrix containing processing additives. **Ceramics International**, v. 35, n. 4, p. 1545–1552, 2009.

[47] LEROUX, L. et al. Effects of various adjuvants (lactic acid, glycerol, and chitosan) on the injectability of a calcium phosphate cement. **Bone**, v. 25, n. 2 SUPPL. 1, p. 31–34, 1999.

[48] KOMATH, M.; VARMA, H. K. Development of a fully injectable calcium phosphate cement for orthopedic and dental applications. **Bulletin of Materials Science**, v. 26, n. 4, p. 415–422, 2003.

[49] GERHARDT, L. C.; BOCCACCINI, A. R. Bioactive glass and glass-ceramic scaffolds for

bone tissue engineering. **Materials**, v. 3, n. 7, p. 3867–3910, 2010.

[50] KAUR, G. et al. Mechanical properties of bioactive glasses, ceramics, glass-ceramics and composites: State-of-the-art review and future challenges. **Materials Science and Engineering C**, v. 104, p. 109895, 2019;

[51] HENCH, L. L. Bioceramics: from concept to clinic. J Am Ceram Soc. 1993;72:93-98. **Journal of the American Ceramic Society**, v. 74, p. 1487–1510, 1991.

[52] POMPEU, L. L. M. F. et al. Aluminatos de cálcio e seu potencial para aplicação em endodontia e ortopedia. **Ceramica**, v. 59, n. 350, p. 216–224, 2013.

[53] ZAPATA, J. F.; GOMEZ, M.; COLORADO, H. A. Structure-property relation and Weibull analysis of calcium aluminate cement pastes. **Materials Characterization**, v. 134, n. 53, p. 9–17, 2017.

[54] PEREZ, R. A.; KIM, H. W.; GINEBRA, M. P. Polymeric additives to enhance the functional properties of calcium phosphate cements. **Journal of Tissue Engineering**, v. 3, n. 1, p. 1–20, 2012.

[55] SAGHIRI, M. A. et al. Radiopacifier particle size impacts the physical properties of tricalcium silicate-based cements. **Journal of Endodontics**, v. 41, n. 2, p. 225–230, 2015.

[56] CUI, X. et al. An injectable borate bioactive glass cement for bone repair: Preparation, bioactivity and setting mechanism. **Journal of Non-Crystalline Solids**, v. 432, p. 150–157, 2016.

[57] SUBHI, H. et al. Physicochemical, mechanical and cytotoxicity evaluation of chitosan-based accelerated portland cement. **Journal of Materials Research and Technology**, v. 9, n. 5, p. 11574–11586, 2020.

[58] KACHEL-JAKUBOWSKA, M.; MATWIJCZUK, A.; GAGOŚ, M. Analysis of the physicochemical properties of post-manufacturing waste derived from production of methyl esters from rapeseed oil. **International Agrophysics**, v. 31, n. 2, p. 175–182, 2017.

[59] LAWRIE, G. et al. Interactions between alginate and chitosan biopolymers characterized using FTIR and XPS. **Biomacromolecules**, v. 8, n. 8, p. 2533–2541, 2007.

[60] IANOŞ, R. et al. Solution combustion synthesis of strontium aluminate, SrAl2O4, powders: Single-fuel versus fuel-mixture approach. **Physical Chemistry Chemical Physics**, v. 18, n. 2, p. 1150–1157, 2015.

[61] CASTILLA-CASADIEGO, D. A. et al. Design, characterization, and modeling of a chitosan microneedle patch for transdermal delivery of meloxicam as a pain management strategy for use in cattle. **Materials Science and Engineering C**, v. 118, n. August 2020, p. 111544, 2021.

[62] TARTE, P. Infra-red spectra of inorganic aluminates and characteristic vibrational frequencies of AlO4 tetrahedra and AlO6 octahedra. **Spectrochimica Acta Part A: Molecular Spectroscopy**, v. 23, n. 7, p. 2127–2143, 1967.

[63] ESPANOL, M. et al. Intrinsic porosity of calcium phosphate cements and its significance for drug delivery and tissue engineering applications. **Acta Biomaterialia**, v. 5, n. 7, p. 2752–2762, 2009.

[64] ZHANG, J. et al. Calcium phosphate cements for bone substitution: Chemistry, handling and mechanical properties. **Acta Biomaterialia**, v. 10, n. 3, p. 1035–1049, 2014.

[65] VEZENKOVA, A.; LOCS, J. Sudoku of porous, injectable calcium phosphate cements – Path to osteoinductivity. **Bioactive Materials**, v. 17, n. January, p. 109–124, 2022.

[66] ACUÑA-GUTIÉRREZ, I. O. et al. Development of LiCl-containing calcium aluminate cement for bone repair and remodeling applications. **Materials Science and Engineering C**, v. 70, p. 357–363, 2017.

[67] LODE, A. et al. Strontium-modified premixed calcium phosphate cements for the therapy of osteoporotic bone defects. **Acta Biomaterialia**, v. 65, p. 475–485, 2018.

[68] DAI, J. et al. A novel and injectable strontium-containing hydroxyapatite bone cement for bone substitution: A systematic evaluation. **Materials Science and Engineering C**, 2021.